

Comprehensive study on the structural and optical properties of bismuth manganese oxide composite ceramic for optoelectronic applications

P. P. NAYAK¹, B. SWAIN¹, R. R. PATRO², S. S. HOTA³, O. P. DAS¹, and S. BHUYAN¹

Received date:

9 May 2025

Revised date:

29 July 2025

Accepted date:

25 September 2025

Keywords:

XRD;

FTIR;

Urbach energy;

Sillenite;

Mullite

Abstract

This work assessed the potential of bismuth manganese oxide composite ceramic for optoelectronic applications by methodically examining its structural, vibrational, and optical characteristics. X-ray diffraction (XRD) spectroscopy provided the coexistence of Bi₁₂MnO₂₀ (sillenite-type) and Bi₂Mn₄O₁₀ (mullite-type) phases, indicating a deviation from the ideal perovskite structure and suggesting a complex crystallographic nature influencing its functional properties. Fourier transform infrared (FTIR) spectroscopy confirmed the modes of vibration of Bi-O and Mn-O bonds that were contained, supporting the structural composition. UV-Vis-NIR spectroscopy demonstrated strong optical absorption in the 300 nm to 800 nm range, affirming the suitability of the material for optoelectronic applications. The bandgap energy was determined to be 3.091 eV, with Tauc's analysis revealing direct transitions at 0.66 eV and 5.15 eV and indirect transitions at 1.11 eV and 5.17 eV, suggesting multiple electronic absorption mechanisms. The Urbach energy of 3.34 eV indicated significant structural disorder due to composite nature and lattice distortions. Additionally, extinction coefficient and penetration depth analysis confirmed strong lightmatter interaction, reinforcing potential properties for optical coatings, photodetectors, and energyharvesting applications.

1. Introduction

Transition metal oxides with perovskite structures have been widely studied because of their remarkable magnetic, structural, and electrical characteristics. Strong interactions between the degrees of freedom for spin, charge, and lattice in these materials result in remarkable physical properties such as multiferroicity, magnetoresistance, and superconductivity. Among them, bismuth-based perovskites have gained considerable interest in their potential applications in multipurpose electronic devices, owing to the unique stereo chemical activity of Bi3+ ions, which induces structural distortions and enhances their electronic properties [1,2]. Many lead free ceramics were also used in electronic and multifunctional devices [3-8].

Bi₁₂MnO₂₀ is a sillenite-type manganese bismuth oxide featuring a cubic I23 crystal structure formed by Mn⁴⁺O₄ tetrahedrons within a bismuth-oxygen matrix, with a typical lattice parameter near 10.15 Å and possible coexistence with BiMn₂O₅ under certain synthesis conditions [9]. The material's band gap of about 1.66 eV and strong light absorption across UV, visible, and near-infrared regions make it especially attractive for photocatalysis—including visible-lightdriven water splitting and pollutant removal—arising from O 2p-Mn 3d orbital hybridization [10]. Hierarchical microparticles built from nanocubes have enhanced microwave absorption, supporting optoelectronic and photonic applications. Bi₁₂MnO₂₀ also shows superparamagnetic behavior at the nanoscale, as well as Arrheniustype electric relaxation and small polaron hopping conduction with activation energies near 0.4 Ev [11]. Electrical properties include pronounced dielectric dispersion and non-ferroelectric relaxation, differentiating it from conventional bismuth oxides and enabling sensor and composite device possibilities. Synthesis options such as hightemperature solid-state reactions and low-temperature soft-chemical or hydrothermal routes allow morphology control for device integration. Overall, its combined crystal, electronic, and optical properties propel Bi₁₂MnO₂₀ as a multifaceted material for renewable energy, sensors, environmental remediation, and advanced electronics [12].

Bi₂Mn₄O₁₀ is a complex layered manganese bismuth oxide notable for its distorted and asymmetrical coordination around bismuth atoms, which is mainly caused by the stereochemically active 6s² lone electron pair on Bi. This lone pair contributes to crystal lattice distortions that strongly influence the material's electronic and magnetic properties. Structurally, Bi₂Mn₄O₁₀ has a unique arrangement of MnO₆ octahedra interconnected in layers, which gives rise to interesting antiferromagnetic transitions and magnetic behaviors. These magnetic properties can be further tuned by doping with elements such as chromium and cobalt, which modify magnetic ordering and electrical conductivity, demonstrating the material's potential for magnetic and electronic applications. Synthesized typically by solid-state reactions at high temperatures, this material's phase purity and composition can be controlled to optimize physical properties. The combination of bismuth's lone pair-driven distortion and manganese's magnetic interactions

¹ Faculty of Engineering and Technology, SOA University, BBSR-751030, India

² Department of Computer science and Information technology, GITA Autonomous College, Bhubaneswar, India

³ Physics department, SOA University, BBSR-751030, India

^{*}Corresponding author e-mail: omprakashdas@soa.ac.in

2 NAYAK, P. P., et al.

results in electrical resistivity variations, metamagnetic transitions, and spin reorientation phenomena, making Bi₂Mn₄O₁₀ a promising candidate for multifunctional electronic, magnetic, and sensor devices. Its distinctive structure-function relationship places it among advanced layered oxides with potential in next-generation magnetoelectronic components and novel ceramic materials [13,14].

Combination of $Bi_{12}MnO_{20}$ — $Bi_{2}Mn_{4}O_{10}$ phase may also contributes towards optoelectronic and many related device applications. In this work, we aim to bridge this gap by conducting a systematic structural and optical investigation of bismuth manganese oxide composite ceramic material ($Bi_{12}MnO_{20}$ — $Bi_{2}Mn_{4}O_{10}$). We examine its optical response and crystallographic characteristics using Fourier transform infrared (FTIR) measurements, UV-Vis spectroscopy, and X-ray diffraction (XRD). By correlating its structural characteristics with optical behaviour, this study seeks to provide new insights into its electronic transitions, absorption characteristics, and suitability for multifunctional optoelectronic and magneto-optical applications. This research will not only enhance the fundamental understanding of the composite but also pave the way for its integration into next-generation optoelectronic devices.

2. Experimental analysis

The material Bi₁₂MnO₂₀–Bi₂Mn₄O₁₀ phase was synthesized using the high-temperature ceramic fabrication method known as solid-state reaction (SSR). High-purity Bismuth(III) Oxide (Bi₂O₃) (99.5%) and Manganese Oxide (MnO₂) (99%), sourced from M/S Loba Chemie Co., were subjected to extensive dry grinding for 4 h, followed by wet grinding with ethanol for to get a uniform mixture, using an agate mortar and pestle for 2 h. The uniform powdered sample was then placed in a preheated high-temperature muffle furnace at 850°C for 5 h (heating rate: $3^{\circ}\text{C·min}^{-1}$) inside a high-purity alumina crucible with a cover. This calcination step facilitated the decomposition of starting reagents and the removal of volatile substances. Prior to X-ray diffraction (XRD) analysis, the calcined mixture was further ground (dry and wet) to improve homogeneity and reduce grain size. The XRD pattern was obtained across a wide range of Bragg angles (20° \leq 20



Figure 1. Process flow of SSR method of $Bi_{12}MnO_{20}$ – $Bi_2Mn_4O_{10}$ sample.

≤80°) using a Rigaku Ultima Japan diffractometer with Cu Kα radiation $(\lambda = 1.5405 \text{ Å})$. Phase identification and structural analysis, including the determination of the crystal system, unit cell lattice parameters, and Miller indices, were performed using X'pert Highscore software. After confirming the successful formation of BiMnO₃ via XRD, the material was subjected to FTIR spectroscopy (FT/IR-4600 spectrometer) and pelletization. A portion of the sample was compacted using a KBr hydraulic press at 4 × 106 N·m⁻² of pressure for approximately 4 min to 5 min to form cylindrical pellets that are 12 mm in diameter and 1 mm to 3 mm thick. These pellets were then sintered in a covered alumina crucible at 900°C for 4 h. The properties of the material were then assessed using a variety of characterizations on the sintered, closely packed pellet. Furthermore, The UV-Vis spectroscopy (V-670 spectrophotometer) was used to examine the optical characteristics of the powdered sample. Figure 1 demonstrates the process flow for this experimental work.

3. Results and analysis

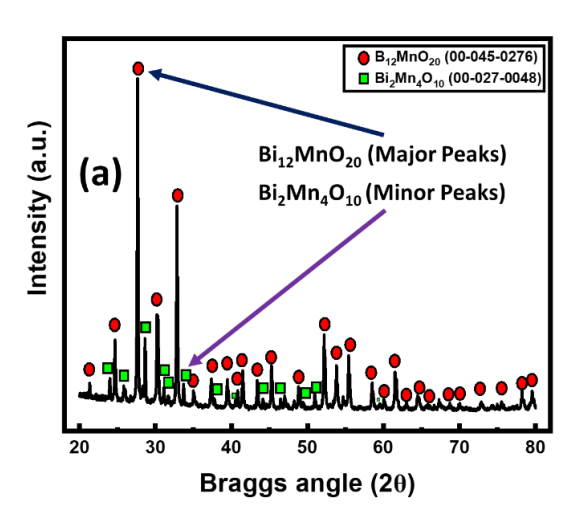
3.1 Structural study

The diffraction pattern that was recorded is displayed in Figure 2(a). was analyzed using X'Pert HighScore software, where the peak positions and intensities were compared with conventional reference patterns to determine the crystalline phases present in the sample. XRD analysis of the synthesized sample revealed the presence of multiple phases. The primary phase was identified as Bi₁₂MnO₂₀ (Reference code: 00-045-0276), with a majority of the detected peaks aligning with its standard diffraction pattern. Additionally, a secondary phase, Bi₂Mn₄O₁₀ (Reference code: 00-027-0048), was observed, contributing to a smaller fraction of the overall diffraction peaks. The presence of these secondary phases suggests that the synthesis process led to partial phase segregation, potentially due to thermal decomposition at elevated temperatures.

The crystallite size and microstrain were estimated using the Williamson-Hall (W-H) approach [15]. The technique is predicated on the idea that both finite crystallite size and lattice strain contribute to the widening of X-ray diffraction (XRD) peaks. The following relation provides the total broadening (β) of the diffraction peaks:

$$\beta \cos \theta = \frac{K\lambda}{D} + 4\epsilon \sin \theta \tag{1}$$

Where β is the full width at half maximum (FWHM) of the diffraction peaks, λ is the X-ray wavelength (1.5405 Å for CuK α), θ is the Bragg angle, ϵ is the micro-strain, and D is the size of the crystallite. The crystallite size can be obtained from the y-intercept and the microstrain of the slope by fitting the plot of $\beta\cos\theta$ versus $4\epsilon\sin\theta$ linearly. Figure 2(b) displays a linear trend in the W-H plot, suggesting that both crystallite size and micro-strain influence peak broadening. From the linear fit, the average crystallite size was found to be 25.99 nm, suggesting the nanoscale crystallinity of the sample. The calculated micro-strain was -0.00588, indicating slight lattice contraction. The negative strain value suggests that material presence compressive lattice strain. The presence of micro-strain can influence the functional properties. Further refinement of synthesis parameters, such as calcination and sintering conditions, may help reduce lattice strain and improve phase purity.



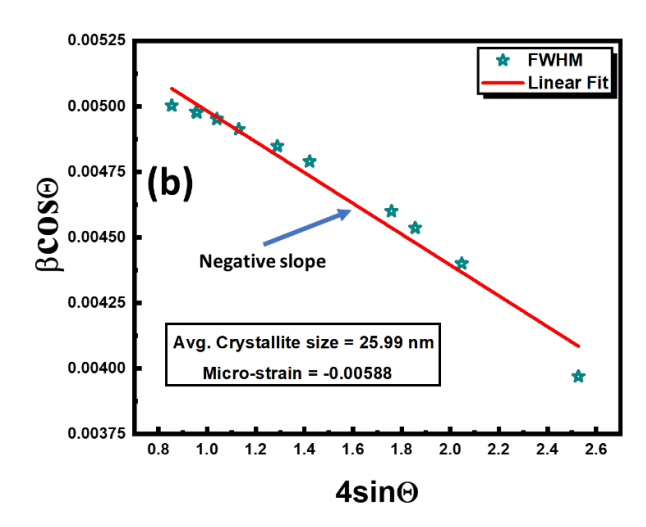


Figure 2. (a) X-ray diffraction pattern (red circles: B₁₂MnO₂₀ and green squares: Bi₂Mn₄O₁₀), and (b) Williamson-Hall plot.

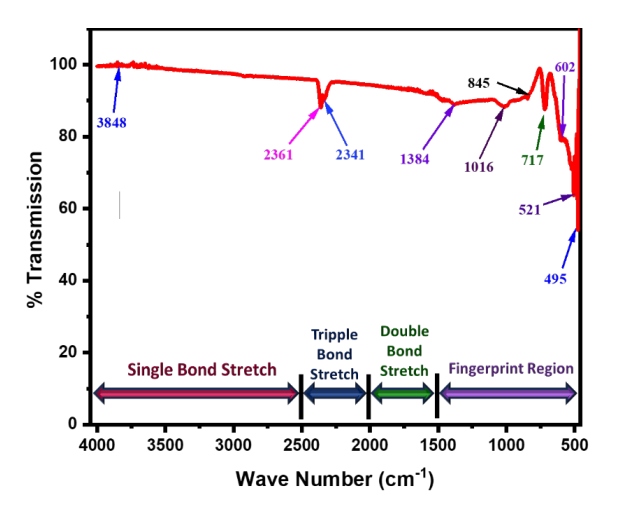


Figure 3. FITR spectra of Bi₁₂MnO₂₀-Bi₂Mn₄O₁₀ sample.

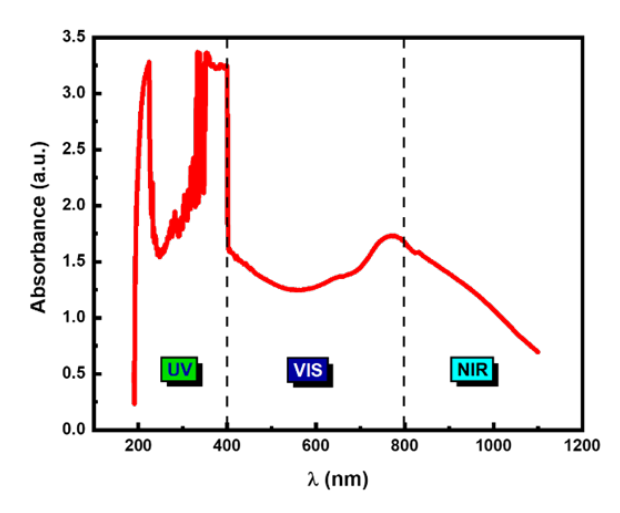


Figure 4. UV-VIS-NIR absorbance spectra versus wavelength of the synthesized sample

3.2 FTIR study

Figure 3 illustrates the vibrational modes of the functional groups in the synthesized sample, which were examined using FTIR spectroscopy. This technique provides crucial insights into the bonding structure

and phase composition of metal oxides, enabling the identification of characteristic absorption bands [16]. The FTIR spectrum aids in confirming the structural integrity of the material while also detecting the presence of secondary phases, moisture, and residual precursors [17]. A broad absorption band observed at 3848 cm⁻¹ corresponds to the stretching vibrations of hydroxyl (O-H) groups, which likely originate from adsorbed moisture on the surface of the sample [18]. The presence of a peak at 2361 cm⁻¹ is associated with CO₂ absorption from atmospheric exposure during sample handling [19]. Additionally, the absorption feature at 2341 cm⁻¹ suggests the presence of carbonate groups, potentially formed due to residual precursors or environmental interactions [20]. The asymmetric stretching of nitrate (NO³⁻) groups is responsible for the peak at 1384 cm⁻¹, suggesting potential synthesisrelated residues [21]. Another notable absorption band at 1016 cm⁻¹ corresponds to Mn-O stretching vibrations, confirming the presence of metal-oxygen bonds, a crucial signature of perovskite-type oxides [22]. The absorption at 717 cm⁻¹ is linked to Bi–O stretching vibrations, which is a characteristic feature of bismuth-based oxides and supports the formation of the sample [23].

In the lower wavenumber region, the bands at 602 cm⁻¹, 521 cm⁻¹, and 495 cm⁻¹ correspond to Bi–O and Mn–O stretching modes, confirming the structural framework of the sample [24]. These observations align well with previous studies on Bi- and Mn-based perovskite oxides [25]. The minor peaks at higher wavenumbers suggest the presence of residual moisture, carbonate, or nitrate groups, which could have been introduced during synthesis or sample storage [26]. Overall, the FTIR analysis confirms the formation of Bi₁₂MnO₂₀–Bi₂Mn₄O₁₀ sample with distinct Bi–O and Mn–O stretching bands while also indicating minor contributions from secondary phases.

3.3 UV study

3.3.1 Optical absorbance and bandgap energy

Figure 4 presents the UV-Vis-NIR absorbance spectrum of the synthesized material, displaying notable absorption across the ultraviolet (UV) and visible (Vis) regions, extending up to approximately 800 nm. This broad absorption suggests as an effective photocatalyst under both UV and visible light irradiation. The characteristics align with

previous studies on bismuth manganese oxide samples synthesized via hydrothermal methods, which also reported enhanced absorbance in the 300 nm to 800 nm range [27]. Such optical properties highlight suitability for applications in photo catalysis and optoelectronic devices.

The thickness (d) and absorbance (A) were used to compute the optical absorption coefficient (α) of the pallet using the following law [28]:

$$\alpha = \frac{2.303 \times A}{d} \tag{2}$$

The α fluctuation and derivative behaviour, $d\alpha/d\lambda$ with λ , are shown in Figure 5(a-b). By applying the experimental technique, we may determine the wavelength that corresponds to the band gap by figuring out the smallest value of $d\alpha/d\lambda$ (E_g). The following formula is then used to determine the band gap energy [29]:

$$E_{\rm g} = hv = \frac{hc}{\lambda} \tag{3}$$

where c is a constant i.e. 3×10^8 m·s⁻¹, h = 4.135×10^{-15} eV·s⁻¹. We can determine the wavelength value λ , which corresponds to 404.035 nm, from the curve da/d λ . We determined the band gap ($E_{\rm g}$) using Equation (3), and the result was $E_{\rm g} = 3.091$ eV. Moreover, the band gap value may also be inferred from the derivative plot of the

reflectance measurement example, which is displayed in Figure 5(c) [30]. It is interesting to note that, as shown in the inset of Figure 5(b), the band energy $E_{\rm g}$ value derived from the maximum of the dR/d λ plot agrees well with the value determined from the d α /d λ spectra. As stated [31,32], Tauc's theory was then used to compute the value of $E_{\rm g}$ more accurately.

$$(\alpha h v) = \beta (h v - E_g)^n \tag{4}$$

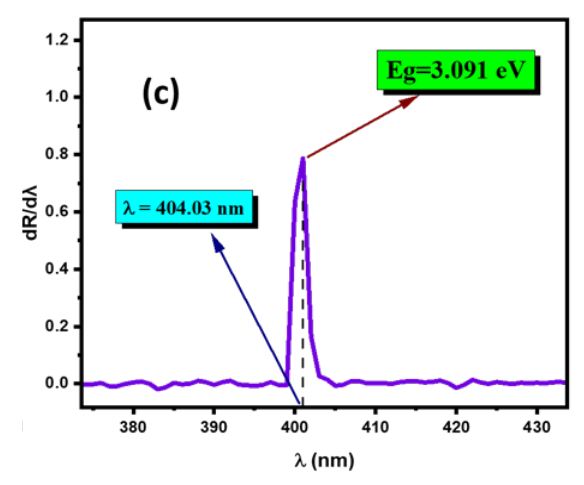
Using Tauc's law, the band gap energy for the synthesized material is now determined as follows:

$$(\alpha h v)^{1/n} = \beta (h v - E_g) \tag{5}$$

where the photon energy is represented by hv, the bandgap energy by $E_{\rm g}$, and the degree of disorder in the molecule is described by β . The exponent n represents different types of electronic transitions, as shown in Table 1 below.

Table 1. Types of electronic transition.

Types of electronic transition	n
Direct-allowed transition	2
Indirect-allowed transition	1/2



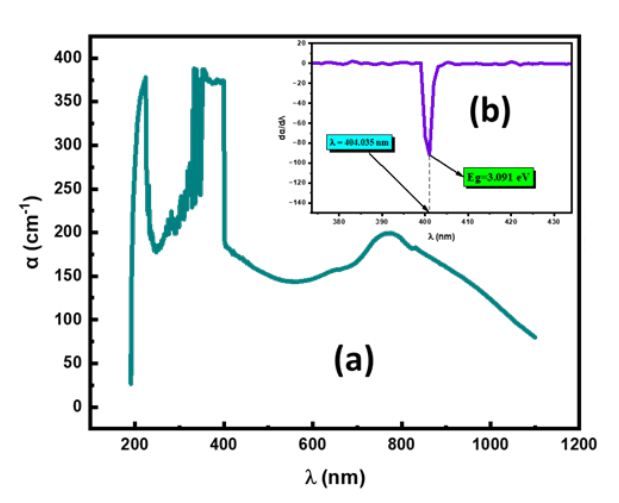
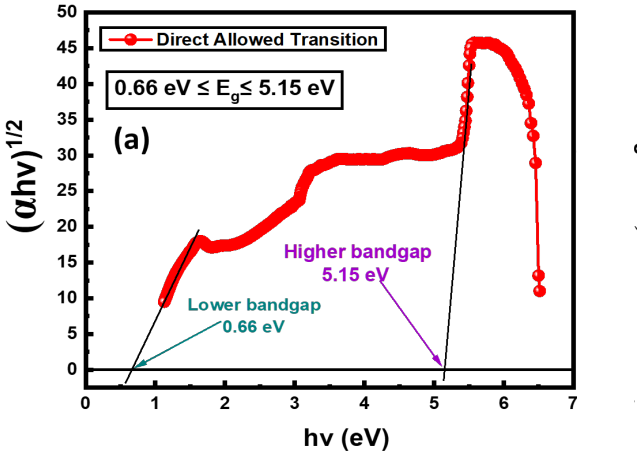


Figure 5. (a) Absorption coefficient (α) vs wavelength, (b) $d\alpha/d\lambda$ vs λ , and (c) $dR/d\lambda$ vs λ .



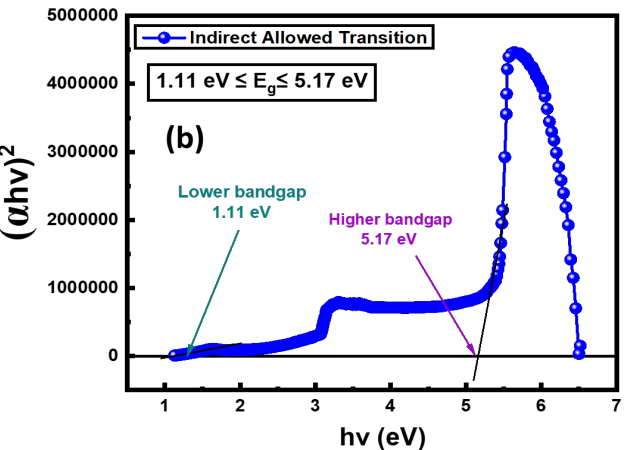


Figure 6. Plots of $(\alpha h v)^{1/2}$ and $(\alpha h v)^2$ versus ho in (a) direct allowed transition, and (b) indirect allowed transition, respectively.

The Tauc's equations for direct and indirect transitions are shown below.

For direct-allowed transition:

$$(\alpha h v)^{1/2} = \beta (h v - E_g) \tag{6}$$

For Indirect-allowed transition:

$$(\alpha h v)^2 = \beta (h v - E_g) \tag{7}$$

Here, we can determine the bandgap energy values for the above electronic transitions. The values of which can be found by using the linear regions of the below graphs plotted in Figure 6(a-b).

The optical properties of the composite were analyzed using Tauc's method for different electronic transitions. The direct allowed transition plot suggests two distinct bandgap values at 0.66 eV and 5.15 eV, while the indirect allowed transition reveals bandgaps at 1.11 eV and 5.17 eV. These variations indicate the presence of multiple absorption mechanisms, potentially linked to different electronic states. The lower bandgap values correspond to intra-band transitions, whereas the higher bandgap values align with fundamental electronic transitions in the material. The observed transitions can be correlated with $\pi \rightarrow \pi^*$ and $n \rightarrow \pi^*$ transitions, where $\pi \rightarrow \pi^*$ transitions arise due to electron excitations within the same bonding-antibonding molecular orbitals. In contrast, $n\rightarrow\pi^*$ transitions occur due to electron movement from a non-bonding state to an antibonding π^* state, influencing optical absorption behaviour. Similar bandgap variations have been observed in previous studies on bismuth manganite and related perovskite oxides, demonstrating their tuneable electronic properties suitable for optoelectronic applications [33-37].

Now, Equation (4) can be rewritten as follows:

$$(\alpha h v) = \ln(\beta) + n \ln(h v - E_g)$$
 (8)

Considering the linear fit of $[\ln (\alpha hv)]$ and $\ln (hv - E_g)$ curves for both the transitions in Figure 7(a-b). The exponent value is close to

0.5 for our sample. The $Bi_{12}MnO_{20}$ – $Bi_{2}Mn_{4}O_{10}$ sample consequently displays a direct optical transition.

3.3.2 Urbach energy

The degree of impurities, disorganization, and flaws in a material is measured by an optical parameter called the Urbach energy ($E_{\rm u}$) [38,39]. The following formula [40] can be used to determine this parameter from the photon energy (hv):

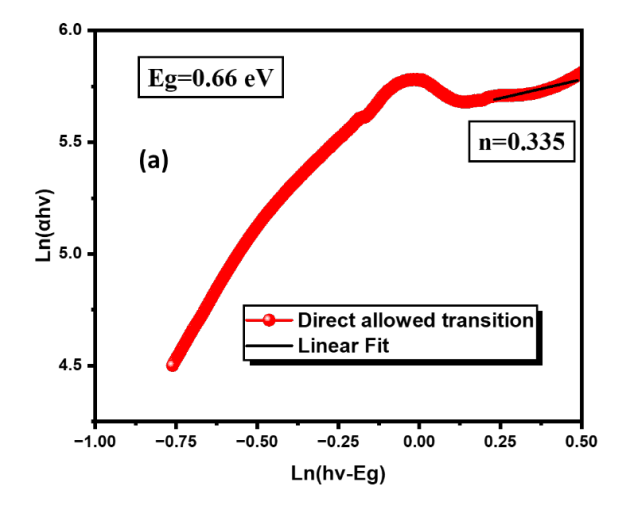
$$\alpha = \alpha_0 \exp\left(\frac{hv}{E_n}\right) \tag{9}$$

where E_u is the Urbach energy, and α_0 is a constant. We established the following relationship by using the logarithmic function on Equation (9).

$$\ln \alpha = \ln \alpha_0 + \left(\frac{h\nu}{E_n}\right) \tag{10}$$

One way to calculate Urbach energy (E_u) is to fit the data linearly, extracting the slope and taking its reciprocal, as shown in Figure 8.

The optical disorder in the sample was analyzed using Urbach energy (E_u) , which characterizes the exponential tail of the absorption edge due to localized states in the bandgap. The slope of the plot $ln(\alpha)$ vs. photon energy (hv) was used to calculate the Urbach energy, which came out to be 3.34 eV. This relatively high $E_{\rm u}$ suggests the presence of significant structural disorder, possibly attributed to oxygen vacancies, grain boundary defects, composite nature or lattice distortions within the perovskite structure. The broadening of the absorption edge indicates strong electron-phonon interactions and localized ionic states, which can influence the optoelectronic properties of the material. Such behaviour is consistent with previously reported Urbach energies in disordered perovskite oxides, highlighting the role of composites in governing the optical absorption characteristics of the material. Given its optical absorption properties and electronic structure, Bi₁₂MnO₂₀-Bi₂Mn₄O₁₀ holds potential for applications in photovoltaics, photocatalysis, and optoelectronic devices, where composite based absorption can play a crucial role in tuning performance.



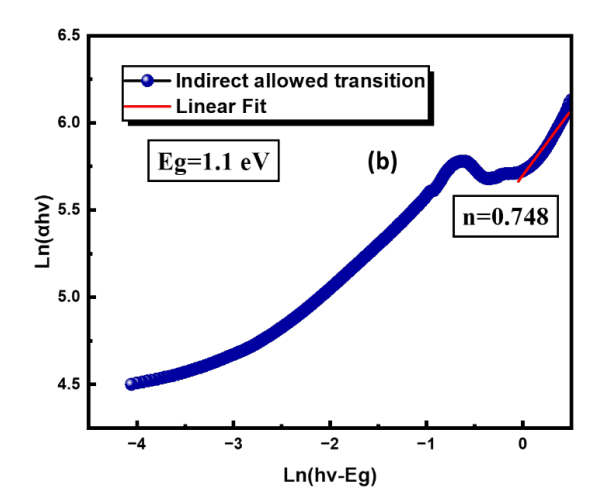


Figure 7. (a) $ln (\alpha h\nu)$, and (b) $ln (h\nu - E_g)$ vs $ln (\alpha h\nu)$ of the synthesized material.

6 NAYAK, P. P., et al.

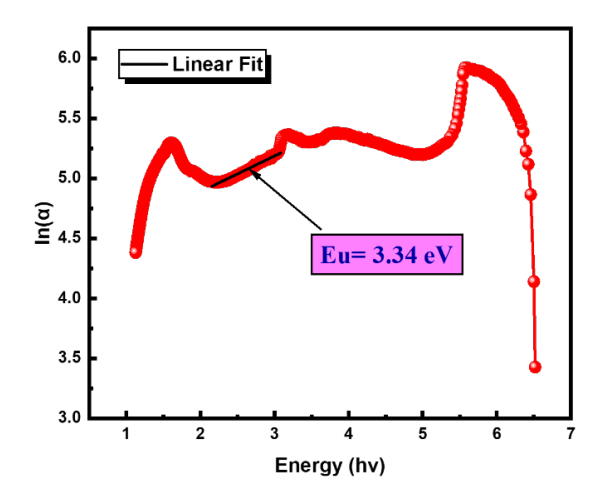


Figure 8. Variation of $\ln (\alpha)$ vs hv of synthesized sample.

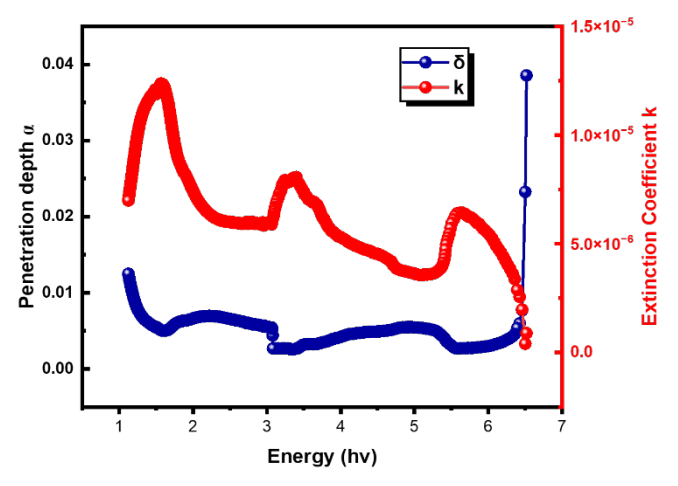


Figure 9. Variation of penetration depth (δ) and extinction coefficient (k) with hv.

3.3.3 Extinction coefficient and penetration depth

The optical properties of $Bi_{12}MnO_{20}$ – $Bi_2Mn_4O_{10}$ are critical for understanding its potential in optoelectronic and photonic applications. Two important parameters that characterize light interaction with the material are the penetration depth (δ) and the extinction coefficient (k).

The strength of the absorption of incident light is described by the extinction coefficient (k), which is correlated with the absorption coefficient (α) [41]. It is given by:

$$k = \frac{\lambda \alpha}{4\pi} \tag{11}$$

where α is the absorption coefficient, and λ is the wavelength of incident light, which is determined from UV-Vis spectroscopy, π is a mathematical constant (\approx 3.1416).

The distance at which incident light intensity drops to 1/e of its initial value is known as the penetration depth (δ) [42]. It is provided by:

$$\delta = \frac{1}{\alpha} \tag{12}$$

Here, the absorption coefficient (α) is a critical parameter in understanding the optical properties of materials, where a higher extinction coefficient (k) indicates stronger optical absorption, while

a greater penetration depth (δ) corresponds to lower absorption. Analyzing the extinction coefficient and penetration depth of the Bi₁₂MnO₂₀–Bi₂Mn₄O₁₀ system over varying photon energies offers valuable insights into its optical behavior, as illustrated in Figure 9. The extinction coefficient (k) exhibits strong absorption in the visible spectral range, which gradually decreases toward the near-infrared region, indicating electronic transitions that mainly govern these absorption characteristics. The inverse relationship between α and δ highlights the material's ability to confine light within thin films, recommending it for optical coatings and photonic devices. Furthermore, the interaction between these optical parameters and the electronic band structure suggests localized energy states within the material, where increased extinction coefficients at specific energy bands indicate enhanced light-matter interactions, which can be exploited for nonlinear optical applications. The capacity to fine-tune penetration depth is especially advantageous in designing Bi-Mn-O-based optoelectronic devices such as photodetectors and solar cells, where efficient photon absorption is paramount. These findings position Bi₁₂MnO₂₀-Bi₂Mn₄O₁₀ as a promising material for next-generation energy harvesting and photonic applications, supported by its tailored optical properties and strong light absorption capabilities.

4. Conclusions

In this study, the structural, vibrational, and optical properties of Bi₁₂MnO₂0-Bi₂Mn₄O₁₀ have been thoroughly investigated. X-ray diffraction (XRD) analysis confirms the presence of two distinct crystallographic phases: Bi₁₂MnO₂₀ (sillenite-type) and Bi₂Mn₄O₁₀ (mullite-type). The presence of Bi₁₂MnO₂₀ suggests potential photonic applications, while Bi₂Mn₄O₁₀ could contribute to catalytic and optical functionalities. The W-H analysis reveals nanoscale crystallinity (25.99 nm) in the sample, with a negative micro-strain (-0.00588), indicating compressive lattice strain in the composite. FTIR spectroscopy further supports the structural findings by identifying key vibrational modes associated with Mn-O and Bi-O bonds. These characteristic absorption bands validate the composition of the material and provide insight into the bonding environment of the material. The UV-Vis-NIR absorbance spectrum of Bi₁₂MnO₂₀–Bi₂Mn₄O₁₀ exhibited strong absorption in the 300 nm to 800 nm range, highlighting its potential for photocatalytic and optoelectronic applications. The optical bandgap, determined using various methods, was found to be 3.091 eV, while Tauc's analysis revealed direct bandgaps at 0.66 eV and 5.15 eV and indirect bandgaps at 1.11 eV and 5.17 eV, indicating multiple absorption mechanisms due to electronic transitions and composite nature. Urbach energy (E_u) was calculated as 3.34 eV, suggesting significant structural disorder influenced by oxygen vacancies and lattice distortions. The extinction coefficient (k) analysis confirmed strong absorption in the visible range, while penetration depth (δ) variations indicated its potential for optical coatings and photonic applications. These findings establish the material as a promising candidate for advanced optoelectronic and energy-harvesting devices.

References

G. Agbeworvi, A. Pakhira, S. Hariyani, W. Zaheer, A. Giem,
J. R. Ayala, and S. Banerjee, "Stereochemical expression of Bi

- 6s 2 lone pairs mediates fluoride-ion (De) insertion in tunnel-structured Bi₂PdO₄ and Bi_{1.6}Pb_{0.4}PtO₄," *Chemical Science*, vol. 16, no. 12, pp. 5129-5141, 2025.
- [2] H. Naganuma, A. Kovacs, T. Harima, H. Shima, S. Okamura, and Y. Hirotsu, "Structural analysis of interfacial strained epitaxial BiMnO₃ films fabricated by chemical solution deposition," *Journal of Applied Physics*, vol. 105, no. 7, 2009.
- [3] D. Panda, S. S. Hota, and R. N. P. Choudhary, "Development of a complex strontium bismuth molybdate material: Microstructural, electrical, and leakage current characteristics for storage and electronic device application," *Materials Research Bulletin*, vol. 174, p. 112727, 2024.
- [4] D. Panda, S. S. Hota, and R. N. P. Choudhary, "Structural, morphological, dielectric, and electrical characteristics of a brownmillerite material for electronic devices: KBiMn₂O₅," *Chemical Physics Impact*, vol. 8, p. 100540, 2024.
- [5] S. S. Hota, D. Panda, and R. N. P. Choudhary, "Structural, dielectric, electrical, leakage current behavior of calcined compound; (Bi_{1/2}Cs_{1/2})(Fe_{1/3}Mn_{1/3}W_{1/3})O₃ for electronic devices," *Transactions on Electrical and Electronic Materials*, vol. 25, no. 3, pp. 280-293, 2024.
- [6] S. S. Hota, D. Panda, L. Biswal, S. Joshi, A. Shukla, and R. N. P. Choudhary, "Effect of milling time on structural and electrical properties of thermomechanically synthesized of Ba_{0.1}(Bi_{0.45}Na_{0.45})TiO₃ nanoceramics for ferroelectric random-access memory device," *Journal of Alloys and Compounds*, vol. 1010, p. 177041, 2025.
- [7] S. S. Hota, D. Panda, and R. N. P. Choudhary, "Structural, dielectric, electrical, and leakage current properties of SrWO₄ for electronic devices," *Journal of the Korean Ceramic Society*, vol. 61, no. 6, pp. 1207-1221, 2024.
- [8] D. Panda, S. S. Hota, and R. N. P. Choudhary, "Development of lead-free defect brownmillerite perovskite ceramic LiBiFeMnO₅ solid solution for electronic devices," *Advanced Engineering Materials*, vol. 26, no. 20), p. 2400010, 2024.
- [9] L. A. S. De Oliveira, J. P. Sinnecker, M. D. Vieira, and A. Pentón-Madrigal, "Low temperature synthesis, structural, and magnetic characterization of manganese sillenite Bi₁₂MnO₂₀," *Journal of Applied Physics*, vol. 107, no. 9, 2010.
- [10] X. Wu, M. Li, J. Li, G. Zhang, and S. Yin, "A sillenite-type Bi₁₂MnO₂₀ photocatalyst: UV, visible and infrared lights responsive photocatalytic properties induced by the hybridization of Mn 3d and O 2p orbitals," *Applied Catalysis B: Environmental*, vol. 219, pp. 132-141, 2017.
- [11] J. Zhao, H. Zhang, and J. Xue, "Hierarchical manganese sillenite Bi₁₂MnO₂₀ microparticles assembled by nanocubes with microwave absorption enhancement," *Ceramics International*, vol. 46, no. 4, pp. 4700-4706, 2020.
- [12] A. Z. Szeremeta, A. Molak, S. Pawlus, J. Koperski, and A. Leonarska, "Electrical properties of epoxy-glue/(Bi₁₂MnO₂₀–BiMn₂O₅) composite," *Journal of Composite Materials*, vol. 52, no. 10, pp. 1305-1315, 2018.
- [13] A. Sarker, A. K. M. Rahman, T. Debnath, and A. Hussain, "Studies on Bi₂Mn₄O₁₀ and it's chromium and cobalt doped series," *Acta Crystallographica Section A: Foundation and Advances*, vol. 73, no. a2, pp. C511-C511, 2017

- [14] M. Burianek, T. F. Krenzel, M. Schmittner, J. Schreuer, R. X. Fischer, M. Mühlberg, and T. M. Gesing, "Single crystal growth and characterization of mullite-type Bi₂Mn₄O₁₀." *International journal of materials research*", vol. 103, no. 4, pp. 449-455, 2012.
- [15] Y. T. Prabhu, K. V. Rao, V. S. S. Kumar, and B. S. Kumari, "X-ray analysis by Williamson-Hall and size-strain plot methods of ZnO nanoparticles with fuel variation," *World Journal of Nano Science and Engineering*, vol. 4, no. 1, pp. 21-28, 2014.
- [16] I. Soudani, K. B. Brahim, A. Oueslati, H. Slimi A. Aydi, and K. Khirouni, "Investigation of structural, morphological, and transport properties of a multifunctional Li-ferrite compound," *RSC advances*, vol. 12, no. 29, pp. 18697-18708, 2022.
- [17] E. Smith, and G. Dent, "Modern raman spectroscopy: A practical approach," John Wiley & Sons, 2019, pp. 1-210.
- [18] M. Singh, T. Paul, P. Pal, A. Sahoo, L. S. Tanwar, N. H. Makani, A. Ghosh, and R. Banerjee, "High ionic conduction and polarityinduced piezoresponse in layered bimetallic Rb₄Ag₂BiBr₉ single crystals," *The Journal of Physical Chemistry C*, vol. 126, no. 51, pp. 21810-21824, 2022.
- [19] Y. Y. Dong, Y. Liang, B. Gao, and Q. Xu, "Supercritical CO2induced plastic deformation on two-dimensional SrZrO3 for its multiferroic performance," *Materials Chemistry Frontiers*, vol. 9, no. 8, pp. 1213-1219, 2025.
- [20] R. Hailili, Z. Q. Wang, H. Ji, C. Chen, X. Q. Gong, H. Sheng, and J. Zhao, "Mechanistic insights into the photocatalytic reduction of nitric oxide to nitrogen on oxygen-deficient quasi-two-dimensional bismuth-based perovskites," *Environmental Science: Nano*, vol, 9, no. 4, pp. 1453-1465, 2022.
- [21] C. Zhang, K. Xu, K. Liu, J. Xu, and Z. Zheng, "Metal oxide resistive sensors for carbon dioxide detection," *Coordination Chemistry Reviews*, vol. 472, p. 214758, 2022.
- [22] U. Manhas, A. K. Atri, S. Sharma, S. Singh, I. Qadir, P. Sharma, M. Sharma, and D. Singh, "High-performance recyclable magnetic CuFe_{2-x} Cr_xO₄ nanocatalysts for facile reduction of nitrophenols and photooxidative degradation of organic dyes," ACS Sustainable Resource Management, vol. 1, no. 2, pp. 303-315, 2024.
- [23] S. Wu, D. Ruan, Z. Huang, H. Xu, and W. Shen, "Weakening Mn–O bond strength in Mn-based perovskite catalysts to enhance propane catalytic combustion," *Inorganic Chemistry*, vol. 63, no. 22, pp. 10264-10277, 2024.
- [24] X. Zheng, L. Zhang, X. Wang, Y. Qing, J. Chen, Y. Wu, S. Deng, L. He, F. Liao, Y. Wang, J. Geng, J. Sun, G. Li, L. Liu, and J. Lin, "Synthesis, structure, and superconductivity of B-site doped perovskite bismuth lead oxide with indium," *Inorganic Chemistry Frontiers*, vol. 7, no. 19, pp. 3561-3570, 2020.
- [25] J. E. R. Rocha, "Catalyseur pérovskite supporté sur des nanofibres de carbone pour une réduction améliorée de l'oxygène," Doctoral dissertation, *Université Paris sciences et lettres*; *Universidad de Guanajuato*, México, 2023.
- [26] F. Sharmin, "Hydrothermal synthesis of rare earth and transition metal co-doped BiFeO₃ and investigation of their photocatalytic performance," Post graduate dissertations (Theses) of Physics (PHY), Bangladesh University of Engineering and Technology, Bangladesh, 2023.
- [27] P. A. Krawczyk, J. Wyrwa, and W. W. Kubiak, "Synthesis and catalytic performance of high-entropy rare-earth perovskite

8 NAYAK, P. P., et al.

nanofibers:(Y_{0.2}La_{0.2}Nd_{0.2}Gd_{0.2}Sm_{0.2}) CoO₃ in low-temperature carbon monoxide oxidation," *Materials*, vol. 17, no. 8, p. 1883, 2024.

- [28] B. Revathi, L. Balakrishnan, S. Pichaimuthu, A. N. Grace, and N. K. Chandar, "Photocatalytic degradation of rhodamine B using BiMnO₃ nanoparticles under UV and visible light irraiation," *Journal of Materials Science: Materials in Electronics*, vol. 31, pp. 22487-22497, 2020.
- [29] H. M. Ghaithan, S. M. Qaid, Z. A. Alahmed, H. S. Bawazir, and A. S. Aldwayyan, "Electronic structure and optical properties of inorganic Pm3m and Pnma CsPbX₃ (X= Cl, Br, I) perovskite: A theoretical understanding from density functional theory calculations," *Materials*, vol. 16, no. 18, p. 6232, 2023.
- [30] R. Mguedla, A. B. J. Kharrat, O. Taktak, H. Souissi, S. Kammoun, K. Khirouni, and W. Boujelben, "Experimental and theoretical investigations on optical properties of multiferroic PrCrO₃ orthochromite compound," *Optical Materials*, vol. 101, p. 109742, 2020.
- [31] A. M. Mansour, "Fabrication and characterization of a photodiode based on 5', 5"-dibromo-o-cresolsulfophthalein (BCP)," *Silicon*, vol. 11, pp. 1989-1996, 2019.
- [32] A. M. Mansour, E. M. El-Menyawy, G. M. Mahmoud, A. A. Azab, and F. S. Terra, "Structural, optical and galvanomagnetic properties of nanocrystalline Se_{51.43}In_{44.67}Pb_{3.9} thin films," *Materials Research Express*, vol. 4, no. 11, p. 115903, 2017.
- [33] G. V. Umoh, J. E. Leal-Perez, S. F. Olive-Méndez, J. González-Hernández, F. Mercader-Trejo, R. Herrera-Basurto, O. Auciello, and A. Hurtado-Macias, "Complex dielectric function, Cole-Cole, and optical properties evaluation in BiMnO₃ thin-films by Valence Electron Energy Loss Spectrometry (VEELS) analysis," *Ceramics International*, vol. 48, no. 15, pp. 22141-22146, 2022.
- [34] J. Chakrabartty, D. Barba, L. Jin, D. Benetti, F. Rosei, and R. Nechache, "Photoelectrochemical properties of BiMnO₃ thin films and nanostructures," *Journal of Power Sources*, vol. 365, pp. 162-168, 2017.

- [35] Y. A. Mikheev, and Y. A. Ershov, "Assignment of the π→ π* and n→ π* transitions to the spectral bands of azobenzene and dimethylaminoazobenzene," Russian Journal of Physical Chemistry A, vol. 92, pp. 1499-1507, 2018.
- [36] A, Sharan, I. An, C. Chen, R. W. Collins, J. Lettieri, Y. Jia, D. G. Schlom, and V. Gopalan, "Large optical nonlinearities in BiMnO₃ thin films," *Applied Physics Letters*, vol. 83, no. 25, pp. 5169-5171, 2003.
- [37] B. Revathi, and N. K. Chandar, "Magnetic field sensing characteristics of rGO/BiMnO3 nanocomposites loaded clad-modified optical fiber sensor," *Journal of Science: Advanced Materials and Devices*, vol. 7, no. 4, p. 100488, 2022.
- [38] S. A., Moyez, and S. Roy, "Thermal engineering of lead-free nanostructured CH₃NH₃SnCl₃ perovskite material for thin-film solar cell," *Journal of Nanoparticle Research*, vol. 20, pp. 1-13, 2018.
- [39] A, Bougrine, A. El Hichou, M. Addou, J. Ebothé, A. Kachouane, and M. Troyon, "Structural, optical and cathodoluminescence characteristics of undoped and tin-doped ZnO thin films prepared by spray pyrolysis," *Materials Chemistry and Physics*, vol. 80, no. 2, pp. 438-445, 2003.
- [40] A. M. Mansour, M. Nasr, H. A. Saleh, and G. M. Mahmoud, "Physical characterization of 5', 5 "-dibromo-o-cresolsulfophthalein (BCP) spin-coated thin films and BCP/p-Si based diode," *Applied Physics A*, vol. 125, pp. 1-11, 2019.
- [41] El A. M. Nahrawy, B. A. Hemdan, A. M. Mansour, A. Elzwawy, and A. B. AbouHammad, "Structural and opto-magnetic properties of nickel magnesium copper zircon silicate nano-composite for suppress the spread of foodborne pathogenic bacteria," *Silicon*, vol. 14, no. 12, pp. 1-16, 2021.
- [42] B. A. Hemdan, A. M. El Nahrawy, A. F. M. Mansour, and A. B. A. Hammad, "Green sol—gel synthesis of novel nanoporous copper aluminosilicate for the eradication of pathogenic microbes in drinking water and wastewater treatment," *Environmental Science and Pollution Research*, vol. 26, pp. 9508-9523, 2019.